ORIGINAL RESEARCH ARTICLE

On the Enhanced Creep Performance in Ti6246 Achieved Through Laser Powder Bed Fusion (LPBF) Processing

PRINCE VALENTINE COBBINAH, SAE MATSUNAGA, YOSHIAKI TODA, RYOSUKE OZASA, TAKUYA ISHIMOTO, TAKAYOSHI NAKANO, TSUTOMU ITO, and YOKO YAMABE-MITARAI

The high susceptibility of the Ti–6Al–2Sn–4Zr–6Mo wt pct (Ti6246) alloy to microstructural changes stands as a challenge when processed by the laser powder bed fusion (LPBF) technology. However, leveraging the capabilities of the LPBF process to successfully control the microstructure (and/or crystallographic texture) of the Ti6246 could improve mechanical properties, particularly at elevated temperatures. In this study, the creep performance (at 500 °C) of Ti6246 fabricated from three different LPBF processing conditions and heat-treated (HT) at 885 °C were investigated. In the as-built state, all the LPBFed-Ti6246 exhibited columnar microstructures with crystallographic lamellar-like microstructure (CLM), a near-single crystal-like microstructure (SCM), and polycrystalline microstructure (PCM) textures, respectively. At low applied stresses (100–300 MPa), diffusional creep was the dominant deformation mechanism and its resistance depended on grain size. The reference β-forged-HT Ti6246, characterized by large equiaxed grains, exhibited the lowest strain rate compared to the columnar microstructure of SX1 (CLM)-HT, SX2 (SCM)-HT, and SX3 (PCM)-HT. Conversely, dislocation slip governed deformation at high applied stresses (400–580 MPa) and its efficacy depended on the α/β interfaces in the microstructures. Disjointed columnar grains in SX1 (CLM)-HT and the deformation of the polycrystalline grains in SX3 (PCM)-HT indicated that the melt pool boundaries were unstable in the LPBFed-Ti6246. SX2 (SCM)-HT exhibited the longest creep life due to the relatively stable melt pool boundaries and the near $< 001 >$ SCM crystallographic texture parallel to the applied stresses. Shallow ductile dimples and tears and the observation of laser scan tracks characterized the fracture surfaces of the LPBFed-Ti6246. These indicated that failure occurred by intergranular ductile fracture resulting from the formation of microvoids at the melt pool boundaries.

https://doi.org/10.1007/s11661-025-07759-8

I. INTRODUCTION

THE Ti–6Al–2Sn–4Zr–6Mo wt pct (Ti6246) alloy is an $\alpha + \beta$ alloy classified under the same group as the Ti–6Al–4V wt pct (Ti64) alloy. One primary advantage of the Ti6246 alloy over the Ti64 is its high susceptibility to microstructural changes, which allows a wide heat treatment processing window. However, this high sensitivity of the microstructure of the Ti6246 could pose a challenge when processed using the laser powder bed fusion (LPBF). This is because the LPBF is an additive manufacturing (AM) process that involves local melting, rapid cooling, remelting of already solidified layers, and a repeated heating cycle during fabrication.[1] This repeated cycle is well known to influence the microstructures of LPBF processed parts significantly.[2]

So far, few studies on Ti6246 have involved the LPBF process.[3–5] Carrozza *et al.*[3] varied input energy density and achieved fully dense Ti6246 using the LPBF

PRINCE VALENTINE COBBINAH, SAE MATSUNAGA, and YOKO YAMABE-MITARAI are with the Department of Advanced Materials Science, Graduate School of Frontier Sciences, The University of Tokyo, 5-1-5 Kashiwanoha, Kashiwa, Chiba 277-8561, Japan. Contact e-mails: p.cobbinah22s@ams.k.u-tokyo.ac.jp, mitarai.yoko@edu.k.u-tokyo.ac.jp. YOSHIAKI TODA is with the Center for Basic Research on Materials, National Institute for Materials Science, 1-2-1 Sengen, Tsukuba, Ibaraki, 305-0047, Japan. RYOSUKE OZASA and TAKAYOSHI NAKANO are with the Division of Materials and Manufacturing Science, Graduate School of Engineering, Osaka University, 2-1 Yamadaoka, Suita, Osaka 565-0871, Japan. TAKUYA ISHIMOTO is with the Division of Materials and Manufacturing Science, Graduate School of Engineering, Osaka University and also with the Aluminium Research Center, University of Toyama, 3190 Gofuku, Toyama 930-8555, Japan. TSUTOMU ITO is with the Department of Mechanical systems Engineering, Faculty of Engineering, Toyama Prefectural University, Kurokawa 5180, Imizu, Toyama, 939-0398, Japan.
Manuscript submitted July 30, 2024; accepted March 26, 2025.

Published online: 10 April 2025

process. The authors also observed prior-β grains of columnar morphology and a martensitic microstructure, with higher input energy density resulting in finer α'' needles in the as-built samples. Furthermore, the as-built samples exhibited substantial ductility but low yield strength. Conversely, post-heat treatments markedly increased the strength of the LPBFed-Ti6246 at the expense of ductility.[4] Peng *et al.*[5] also observed the α'' martensitic microstructure in LPBFed-Ti6246. Heat treatment at 650 °C significantly improved the hardness of the samples owing to the decomposition of the α'' phase to the α and β phases. As reported in the studies mentioned above as well as many other studies on titanium (Ti) $\alpha + \beta$ alloys such as Ti64,[6,7] mechanical behavior primarily depends on formed microstructural features such as phase morphology, the type of precipitate that forms, precipitate size, and distribution.

At elevated temperatures, mechanical behavior is also influenced by the synergistic effects of temperature and applied stress on the Ti alloy. Creep resistance is an example of a high-temperature mechanical property strongly desired in structural materials (*e.g.,* Ti6246) used for aerospace applications. To the best of the authors' knowledge, no previous study has paid attention to the creep performance of Ti6246 processed by the LPBF. In our previous study,[8] we optimized the LPBF process parameters over a wide range and studied their effects on the Ti6246. First, we observed the formation of α/α' phases of varying sizes depending on the LPBF process parameters. Also, the far ends of the investigated parameters, *i.e.,* samples with volumetric energy density (VED) $\geq$ 62.5 J/mm^3 formed columnar microstructures whereas VEDs $\leq$ 30 J/mm^3 formed polycrystalline microstructures. As a progress of our research, the present study evaluates the creep performance of the LPBFed-Ti6246 focusing on three different processing conditions (further details are provided in Section 2). Aside from the different microstructures, the three processing conditions were chosen because of the unique texture they exhibited. Laser power of 360 W at 600 mm/s scan speed (VED = 75 J/mm^3) produced alternating textures termed crystallographic lamellar-like microstructure (CLM), 300 W at 1000 mm/s (VED = 50 J/mm^3) formed a near-single crystal-like microstructure (SCM), and 180 W at 1200 mm/s (VED = 25 J/mm^3) resulted in a polycrystalline crystallographic microstructure-like (PCM). This study is the first to report such unique textures for Ti6246. For further insights and comparison with the LPBFed-Ti6246, the present study also investigated the conventional β-forged Ti6246.

In all, texture is an important property determinant factor that significantly influences creep resistance, hence, serving as a strong motivation for the current study.

Table I. Chemical Composition of Ti6246 Powder

Chemical Element	Ti	Al	Sn	Zr	Mo
Quantity (Mass Pct)	balance	4.67	2.17	3.79	5.14

II. MATERIALS AND METHODS

Gas-atomized Ti–6Al–2Sn–4Zr–6Mo wt pct (Ti6246) powders with spherical morphologies served as starting powders. The chemical composition of the Ti6246 powder is presented in Table I. Rectangular samples of height 40 mm and width 7 mm were fabricated using the EOS M290 M LPBF equipment (EOS GmbH, Germany). Table II summarizes the LPBF process conditions used.

The energy inputs involved in the LPBF process were quantified as volumetric energy density (VED) and defined as follows:

$$\text{VED } (\text{J/mm}^3) = \frac{P}{vdt}. \quad [1]$$

Furthermore, the bidirectional scan strategy along the X-axis with no rotations in subsequent layers was used. Therefore, the scanning direction was in the XY plane, and the build direction was parallel to the YZ plane.

A Ti6246 ingot, with chemical composition detailed in Table III, was β-forged at 1000 °C and served as a reference alloy for comparison with the LPBFed-Ti6246. It is important to note that the chemical compositions of both the starting powder and the forged sample were analyzed using an energy-dispersive X-ray spectroscope (EDS) attached to the scanning electron microscope (SEM). The β-transus temperature of Ti6246 is about 935 °C.[9] Therefore, we anticipate the somewhat non-standard composition of the LPBFed prealloyed Ti6246 powder to result in a reduction of its β -transus temperature by about 20 °C.

In addition, the oxygen (O) and iron (Fe) contents in the samples were analyzed using the LECO TC-436 and the Thermo Scientific iCE 3000 atomic absorption spectrometer, respectively. Table IV presents the results of the O and Fe contents in the LPBFed and forged samples.

The LPBFed and β-forged Ti6246 were heat treated (HT) at 885 °C for 1 hour and air cooled. The samples were then machined into the "dog-bone" shape, as illustrated in Figure 1. Table V summarizes the gage diameter and gage length of the creep samples. The R-type thermocouples were attached to each sample to measure the testing temperature, and the respective elongation was measured using a linear gage. To investigate the occurring transitions of deformation mechanisms during the tensile creep test, the step creep test was performed at 500 °C starting with a 100 MPa stress in air condition. The applied stress was then increased to 200, 300, 400, 500, and 580 MPa. The tensile creep test continued until fracture occurred under 580 MPa. Furthermore, the strain rate and applied stresses were analyzed using the classic Bird-Mukherjee-Dorn equation, and the prevalent deformation mechanisms were estimated.

The JEOL JSM-7200F scanning electron microscope (SEM) equipped with an electron backscatter diffractometer (EBSD), EDS, and backscattered electron (BSE) detector was used to characterize the microstructure of the heat treated, cross section, and fractured

Table II. Ti6246 LPBF Process Conditions

Sample Name	Process Parameters				
	Laser Power, P (W)	Scan Speed, v (mm/s)	Hatch Distance, d (μm)	Powder Layer Thickness, t (μm)	VED (J/mm^3)
SX1 (CLM)	360	800	100	60	75
SX2 (SCM)	300	1000			50
SX3 (PCM)	180	1200			25

Table III. Chemical Composition of β-Forged Sample

Chemical Element	Ti	Al	Sn	Zr	Mo
Quantity (Mass Pct)	balance	5.17	2.32	3.86	5.98

Table IV. O and Fe Contents Analysis in the LPBFed and Forged Ti6246

Ti6246 Sample	Chemical Composition	
	O	Fe
	Pct	Pct
Forged	0.074	0.03
LPBFed	0.113	0.03

Table V. Gage Diameter and Gage Length of Creep Samples

Sample Name	Gage Diameter (mm)	Gage Length (mm)
SX1 (CLM)-HT	2.830	12.960
SX2 (SCM)-HT	2.832	12.991
SX3 (PCM)-HT	2.837	13.053
β-Forged-HT	6.017	30.001

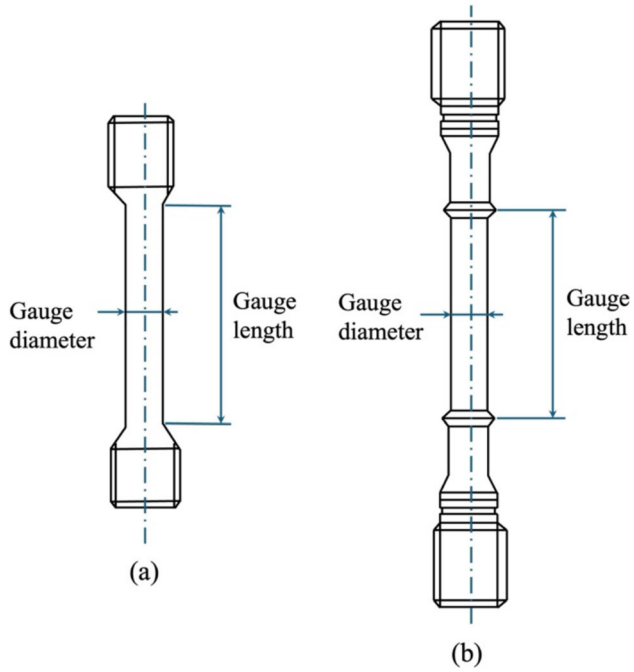

Fig. 1—Schematics of "dog-bone" shape for (*a*) SX1 (CLM)-HT, SX2 (SCM)-HT, and SX3 (PCM)-HT and (*b*) β-forged-HT Ti6246 used for creep tests.

surfaces of all the tested samples. Foremost, the building directions (YZ plane) of all the heat-treated samples and their respective cross sections after the creep testing were mounted, metallographically ground, and polished, with the final stage of polishing involving 0.05 μm colloidal silica for 10 minutes. The EBSD analysis covered minimum areas measuring 300 × 300 μm with a step size of 0.9 μm. The EBSD data were analyzed using the TSL OIM 8 software.

III. RESULTS

A. *Microstructure and Texture of the As-Built Ti6246*

Figure 2(a) through (c) shows the SEM-BSE images of the as-built Ti6246. First, all three samples were fully dense. No defects were observed in SX2 (SCM) and SX3 (PCM). Nevertheless, as depicted in Figure 2(a), SX1 (CLM) exhibited pores due to the high energy input (VED = 75 J/mm^3) applied during the build process. As generally known, these pores result from gas entrapment, which arises from the increased liquid flow velocity (or instabilities) within the melt pool attributable to the high-energy laser input.[10]

Furthermore, the as-scanned microstructures of SX1 (CLM), SX2 (SCM), and SX3 (PCM) exhibited well-defined columnar morphologies in the build direction (Z-direction or YZ plane). Despite typical of the LPBF process, the continuous and defined columnar growths observed in the present study differ from the few reported studies on LPBFed-Ti6246.[3–5] Apart from the obvious difference in process parameters, one possible explanation could be the high laser power employed in the present study. Particularly in SX1 (CLM), the columnar growth occurred in an alternating sequence of thick and thin columnar structures, as depicted in Figure 2(a). The thick columnar structures occurred at the overlapping ends of the melt pools whereas the thin

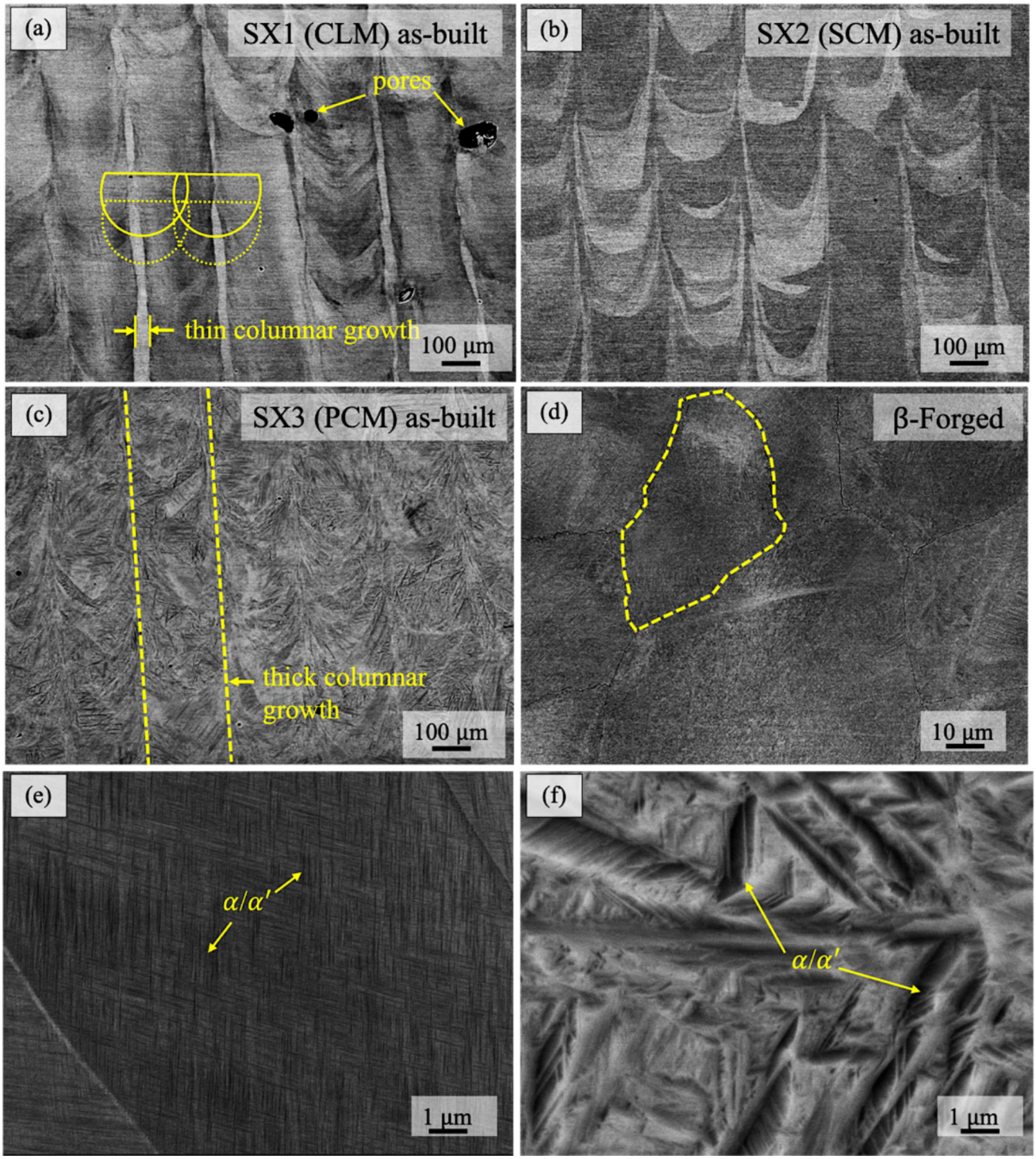

Fig. 2—SEM-BSE images of the as-built LPBFed-Ti6246 (*a*) SX1 (CLM), (*b*) SX2 (SCM), (*c*) SX3 (PCM) observed from the build direction (YZ plane), and (*d*) *β*-forged sample. The magnified SEM images of SX1 (CLM) and SX3 (PCM) are shown in (*e*) and (*f*), respectively.

columnar structures formed and connected at the centers. The defined continuous thick growth at the overlapping ends suggests that during the layer addition process, the localized melting sufficiently remelted the topmost parts of already solidified layers or exceeded the powder layer thickness of 60 μm, promoting the epitaxial growth of existing grains. Concurrently, nucleated new grains at the overlapping ends of the new melt pools also inherited the growth direction through competitive growth leading to the columnar microstructure.

As already reported,[8] the black phases in all the SEM micrographs were identified as the α/α' martensitic phase. In addition, the α'' and ω phases were not

identified in any of the as-built samples. The sizes of the precipitates (α/α' phase) formed in SX1 (CLM) were observed to be extremely refined (in the nanoscale) while those formed in SX3 (PCM) were relatively coarse (microsized). In SX2 (SCM), the sizes were between those of SX1(CLM) and SX3 (PCM). The observed precipitate size differences were mainly attributed to the VEDs used for the respective builds. Readers are referred to our previous study for further insights.[8] On the other hand, the β-forged sample exhibited an equiaxed microstructure with an average grain size of 138 ± 49 μm, as depicted in Figure 2(d). Also, the precipitated α' martensitic phase were refined and of the nanoscale.

Figure 3 shows the EBSD IPF maps of the β- and α/α' martensite phases in the respective as-built Ti6246. In fact, it has been reported that crystallographic texture evolution in the LPBF process largely depends on the melt pool shape, particularly the depth or curvature of the melt pool bottoms.[11] The synergistic effects of the LPBF process parameters account for the differences in melt pool shape, heat flow directions, and consequent crystallographic texture evolution. Analogous to the casting process, the LPBF process forms a non-homogeneous nucleation at the solid phase boundary at the melt pool bottom (or fusion region). The direction of heat flow is fastest perpendicular to the solid–liquid interface, with grains competitively and at the same time preferentially growing along in the opposite direction.[12] As previously mentioned, SX1 exhibited two forms of columnar growths with alternating textures in a lamellar-like pattern observed in the build (YZ plane) and scanning directions (XY plane). This lamellar-like orientation of crystallographic texture has been reported in other studies and is termed as crystallographic lamellar-like microstructure (CLM).[13] The evolution of the CLM texture is usually attributed to the formation of deep melt pools.[13] The high energy input (75 J/mm^3) combined with the X-scan strategy produced deep melt pools and developed significantly high thermal gradients (G) across the scanned layers. Developing deep melt pools and high G increases the tendency to form the $< 001 >$ texture.[14,15] Usually, the primary solidification growth of the β-phase aligns in the $< 001 >$ direction parallel to the build direction and has been reported for many LPBFed β-Ti alloys.[16,17] In the SX1 (CLM) sample, $< 001 >$ thin columnar growths evolved at the center of the melt pools. This is because the center of the melt pools experiences the highest energy and maximum G, promoting preferential or rapid growth of the $< 001 >$ texture across the layers during the build process. Gokcekaya *et al.*[18] postulated that when deep melt pools form, two easy-growth directions perpendicular to each other from the melt pool sides and center occur, which usually results in the $< 001 >$ cubic texture evolution along the build direction. Therefore, the observed different texture at the thick columnar growths indicates that the remelting of the sides of the melt pools affected G, thereby inducing new β orientations and growth.

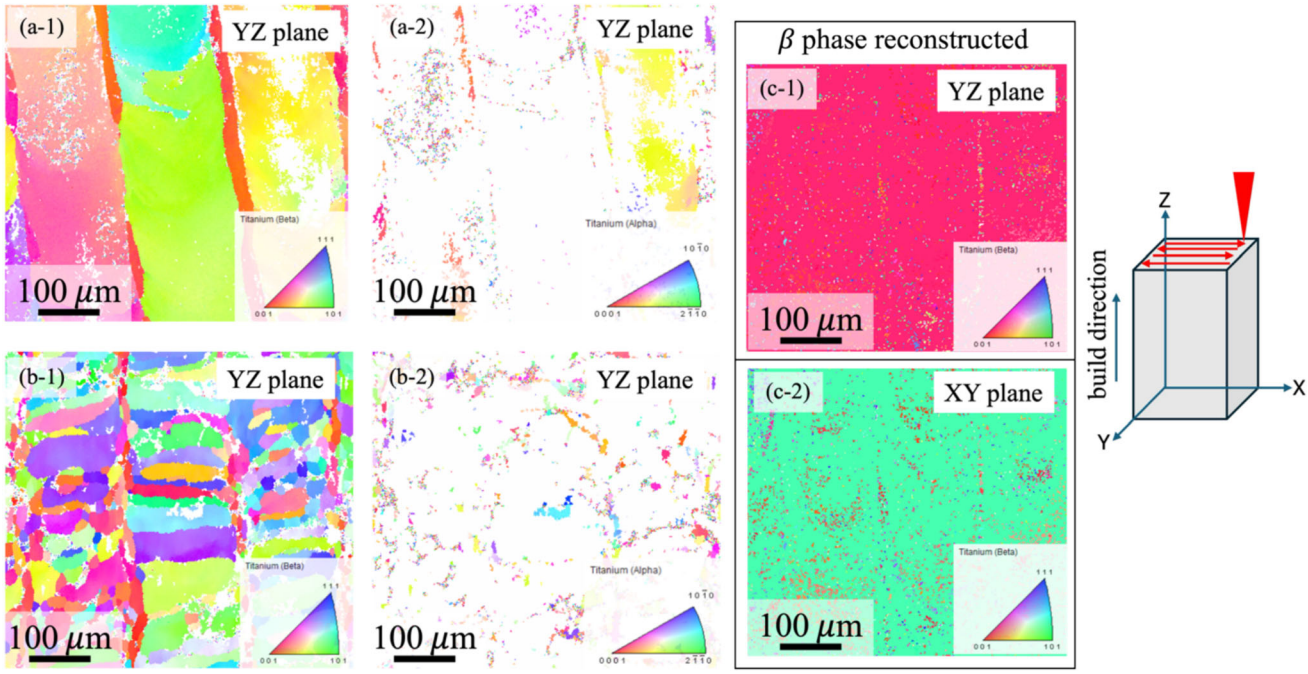

Fig. 3—EBSD IPF maps of (*a-1*) β and (a-2) α/α' martensite phase of the crystallographic lamellar microstructure-like (CLM) in SX1, (*b-1*) β and (*b-2*) $\alpha/\alpha\prime$ martensite phase of the polycrystalline microstructure-like (PCM) in SX3 observed parallel from the build direction (YZ plane), *i.e.,* in the Z-direction; (*c-1*) and (*c-2*) are β-phase reconstructions of the near-single crystal-like microstructure (SCM) in SX2 observed also from the YZ plane and XY plane (scanning direction). [(*b-1*) is reproduced under terms of the Creative Commons CC BY 4.0 license.[8] Copyright 2024, The Authors. Published by Elsevier B.V. on behalf of KeAi Communications Co. Ltd.].

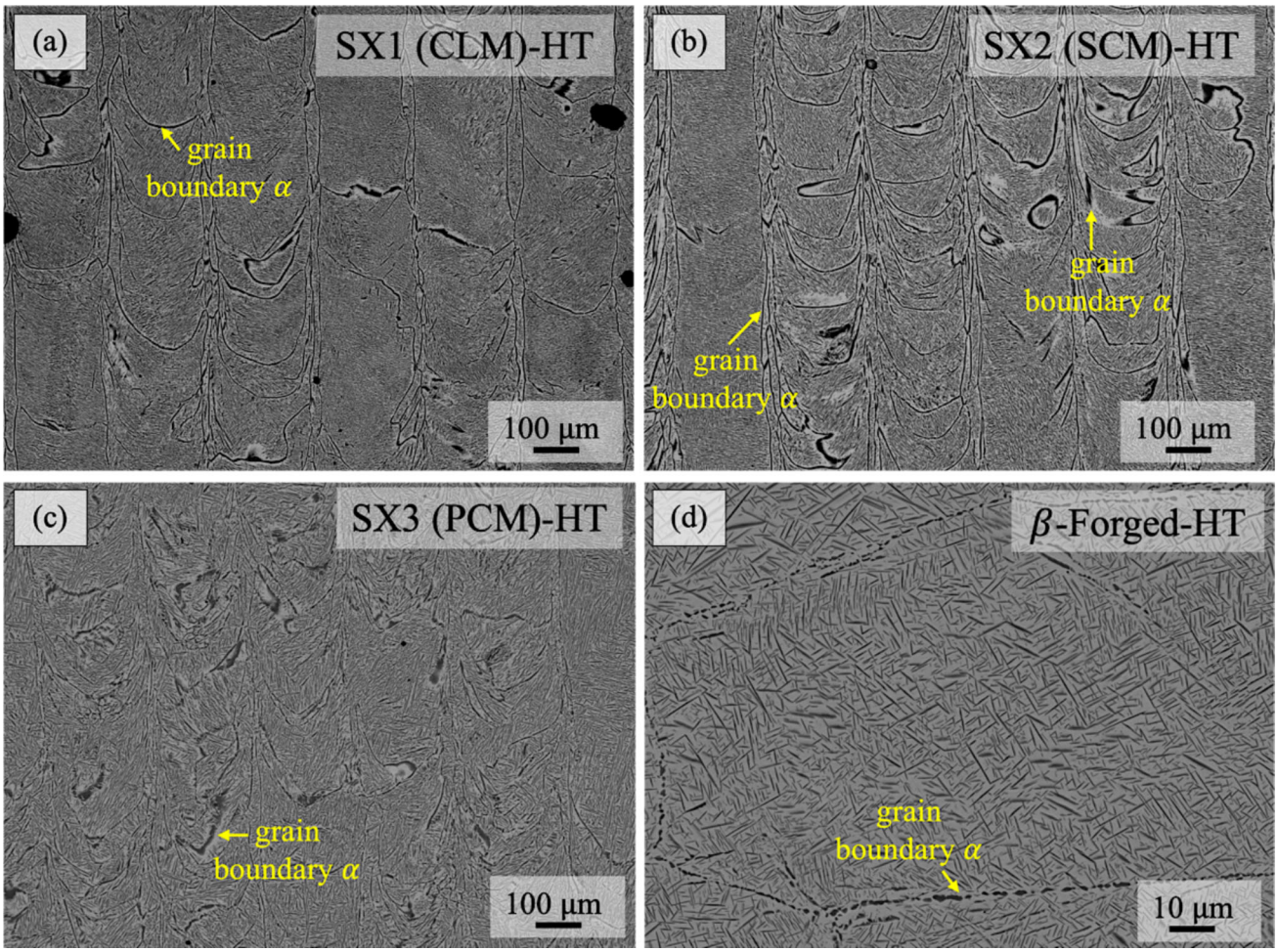

Fig. 4—SEM-BSE images of the heat-treated (HT) LPBFed-Ti6246 (*a*) SX1 (CLM), (*b*) SX2 (SCM), (*c*) SX3 (PCM) observed from the build direction (YZ plane), and (*d*) *β*-forged sample.

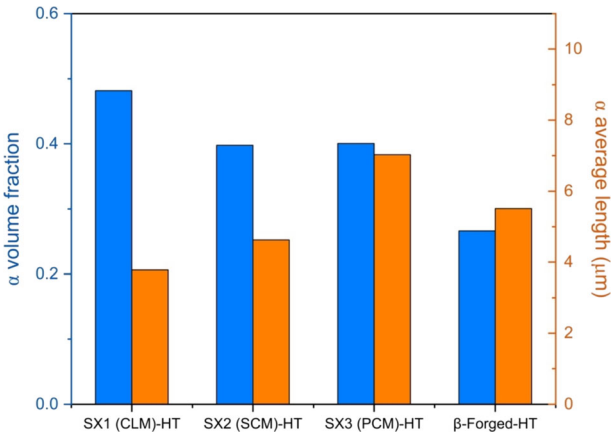

Fig. 5—α phase volume fraction and average length (*μ*m) in the LPBFed and the *β*-forged Ti6246 after heat treatment (HT) at 885 °C for 1 hour and air cooled.

Although the SEM-BSE image of SX3 (PCM) showed a columnar microstructure, the EBSD analysis revealed the polycrystalline crystallographic microstructure (PCM) texture formed in both the build (YZ plane) and scanning (XY plane) directions, as shown in Figure 3(b-1). Unlike SX1 (CLM) and SX2 (SCM), the curvature of the bottom of the melt pools formed in SX3 (PCM) (VED = 25 J/mm^3) significantly decreased owing to both the low laser power input and the fast scan speed. This combination of process parameters prevented the epitaxial growth of grains at the fusion region (or melt pool bottom) and the consequent inheriting of previous crystal orientations. This culminates in the observed randomly oriented small grains in SX3 (PCM).

β-phase reconstruction of texture in SX2 (VED = 50 J/mm^3) revealed a near < 001 > and < 110 > single crystal-like microstructure (SCM) in the build (YZ plane) and scanning (XY plane) directions, as presented in Figures 3(c-1) and (c-2), respectively. The texture in SX2 is referred to as near-SCM because the color observed was pink instead of the typical red color which represents the < 001 > direction. In other words, this perhaps suggests that the direction of grain solidification slightly shifted from the Z-direction. Nevertheless, the columnar microstructure, as evident in Figure 2(b), suggests relatively deep melt pools also formed in SX2 (SCM). From another perspective, the evolution of

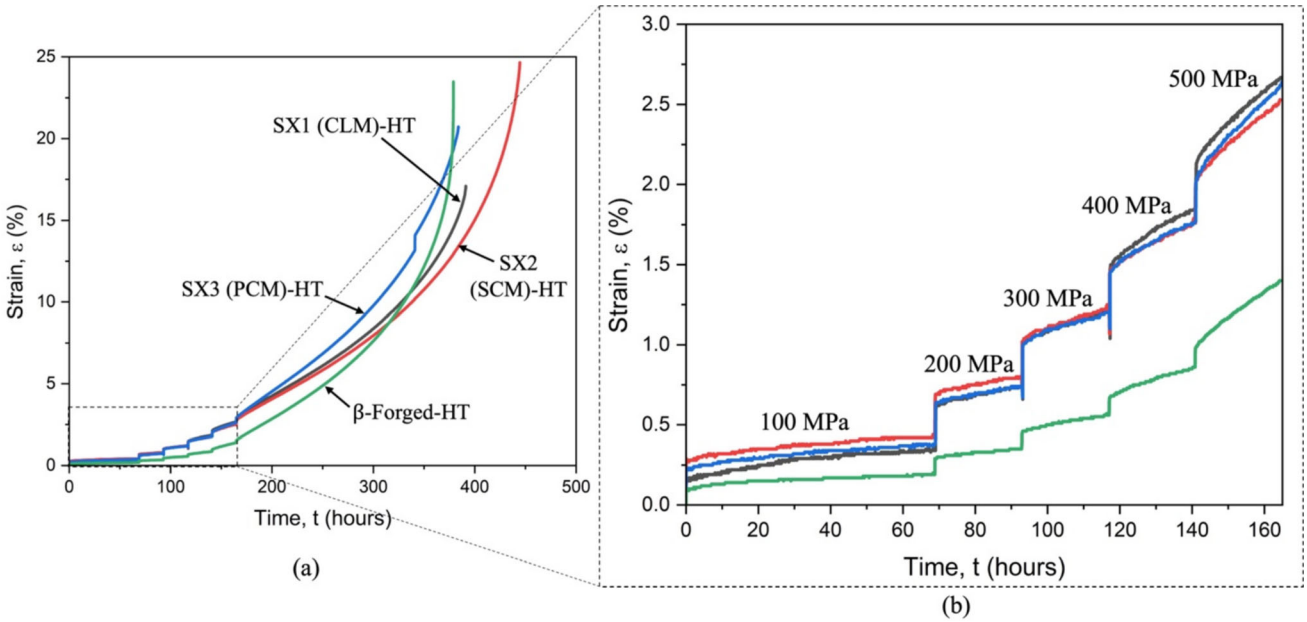

Fig. 6—(*a*) Overall and (*b*) step creep curves of SX1 (CLM)-HT, SX2 (SCM)-HT, SX3 (PCM)-HT, and β-Forged-HT Ti6246 at 500 °C.

the < 001 > texture along the build direction may be attributed to the fixed laser scanning direction employed. Without any rotations, the bidirectional scanning along the X-axis resulted in a homogeneous thermal flux in each melt pool (and layer), ultimately promoting grain preferential growth in the < 001 > direction. Similar texture has been reported for face-centered cubic (fcc) based alloys such as nickel-based superalloys and stainless steels.[11,13,19]

It is worth noting from Figure 3 in the CLM and PCM samples that β texture evolved with relatively few precipitated α/ α' martensites. The effect of solid-state transformation during cooling is one of the biggest challenges in obtaining strong crystallographic texture in ($\alpha+\beta$) Ti alloys with the LPBF process. However, in the present study, we show that with the appropriate LPBF process conditions, the high cooling rates of the LPBF (~ 10^6 K/s) can be used to suppress martensite formation to an extent where crystallographic texture can develop in the ($\alpha+\beta$) Ti alloys. The present study is the first study to successfully obtain β texture in the Ti6246. Also, it is worth adding that Ti6246, by design, contains more equilibrium β phase at room temperature compared to the popularly researched Ti64.[20] The presence of more β phase at room temperature is an important factor that increased the tendency to obtain crystallographic texture in the LPBFed-Ti6246.

B. *Microstructure of the Heat-Treated LPBFed-Ti6246*

Figure 4 shows the SEM-BSE images of the heat-treated (HT) LPBFed and β-forged Ti6246. As expected, the $\alpha\prime$ martensitic phases coarsened and decomposed to the α phase. This is because the decomposition of the $\alpha\prime$ martensitic phase to the α phase is generally diffusion driven, requiring elevated temperature and sufficient time. Foremost, the micrographs provided insight into the locations of the precipitated martensitic phase before heat treatment. The α phase, therefore, was found within the columnar structures and boundaries (longitudinal boundaries and the melt pool boundaries). A closer examination of the micrographs showed that the α phase at the melt pool boundaries (or grain boundaries) was coarser than those found within the columnar structures. The coarsening of the grain boundary α (or grain boundary-like α) after post-processing treatment has been reported in different studies involving LPBFed $\alpha+\beta$ Ti alloys.[21,22]

Similarly, in the β-forged-HT Ti6246, the α phase was located in the equiaxed grains as well as at the grain boundaries. This is in good agreement with available literature on the Ti6246.[23,24]

Figure 5 presents the volume fraction and average lengths of the α phase in the LPBFed and the β-forged Ti6246 after HT. The volume fraction of the α phase in SX2 (SCM)-HT and SX3 (PCM)-HT was about the same (~ 40) after heat treatment. Conversely, the measured average lengths increased from 3.78 μm in SX1 (CLM)-HT to 7.03 μm in SX3 (PCM)-HT. The β-forged-HT Ti6246, on the other hand, exhibited the least α volume fraction (27), but the measured average length (5.5 μm) was between SX2 (SCM)-HT and SX3 (PCM)-HT.

The observed volume fraction and average length variation of the α phase in the LPBFed and the β-forged Ti6246 after HT stemmed from the manufacturing route and process conditions. Especially for SX1 (CLM), SX2 (SCM), and SX3 (PCM), the HT temperature (885 °C) was chosen to maintain the initial morphology and microstructural features obtained from the LPBF process. The variation in volume fraction and average length, thus, resulted from the different VEDs used in LPBFed-Ti6246. As elucidated in our previous study,[8] high density of lattice defects such as dislocations are

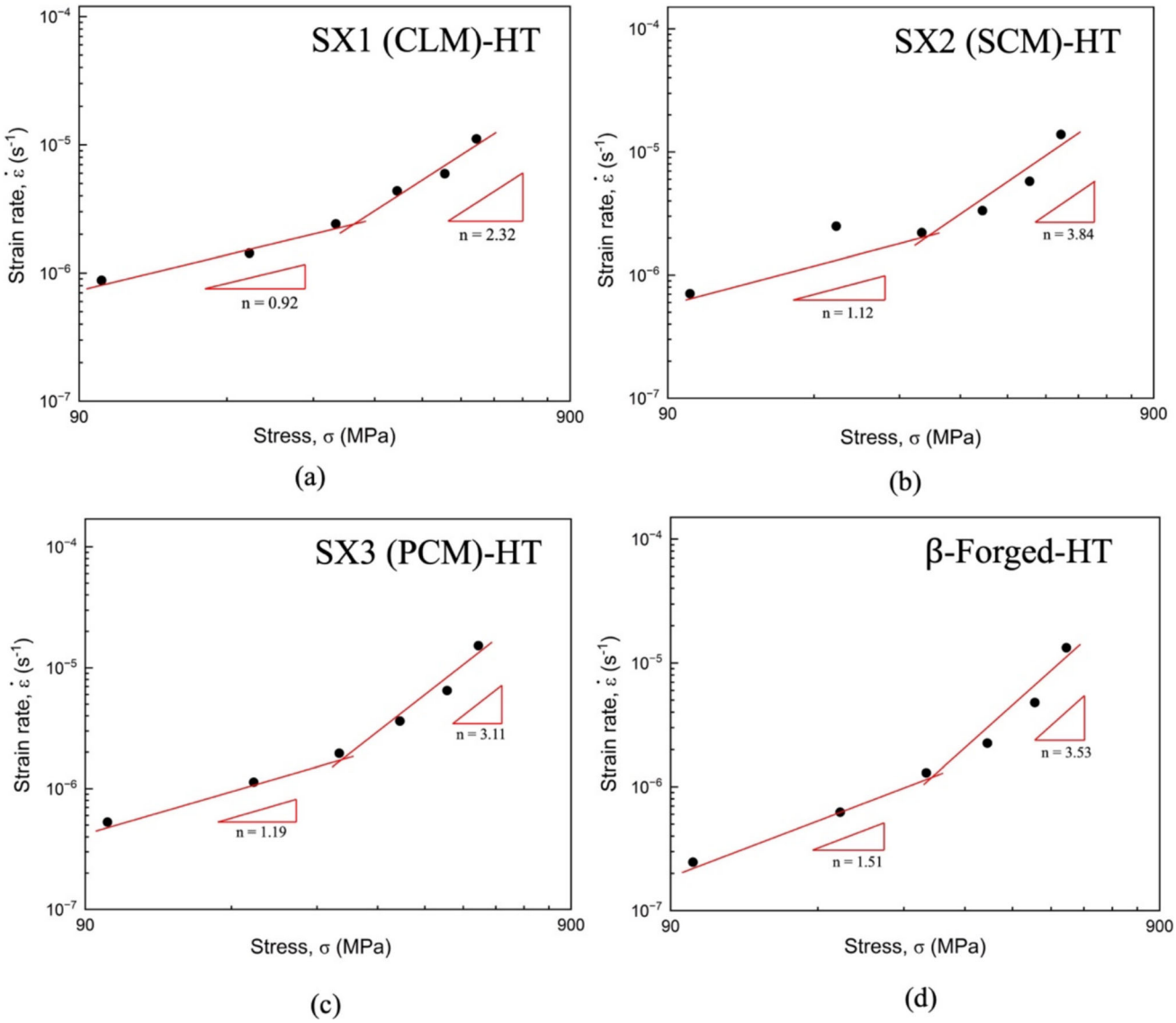

Fig. 7—Dependence of steady-state creep on applied stress at 500 °C in (*a*) SX1 (CLM)-HT, (*b*) SX2 (SCM)-HT, (*c*) SX3 (PCM)-HT, and (*d*) *β*-Forged-HT Ti6246.

generated in the LPBFed-Ti6246. These dislocations assist martensite precipitation and contribute to stress reduction. The number of dislocations increases from the repeated rapid heating and cooling during the deposition of subsequent layers in the LPBF. The presence and increase in dislocation serve as preferential nucleation sites for the martensite and accelerate nucleation rates.[25] Consistent with studies by Yang *et al.*,[26] the available nucleation sites density can be directly related to the applied laser intensity. Thus, the VED of 75 J/mm^3 used in SX1 (CLM) was high and significantly enhanced the nucleation sites, culminating in numerous extremely refined martensites which after HT manifested as the highest α volume fraction and the sample with the least α average length. Compared to the other LPBFed-Ti6246, SX3 (PCM) in the as-scanned state exhibited coarse α/α′ martensites, as shown in Figure 2, owing to the low VED applied. This inevitably explains the highest α average length in SX3 (PCM) after HT even though it shares the same α volume fraction with SX2 (SCM). For the forged reference Ti6246, deformation in the *β* phase (1000 °C) introduced relatively less dislocation densities[27] resulting in the observed lowest α volume fraction.

C. *Creep Behavior of the Heat-Treated LPBFed and β-Forged Ti6246*

Figure 6(a) shows the LPBFed and *β*-forged Ti6246 creep curves. Compared to the HT LPBFed-Ti6246, the β-forged-HT Ti6246, with an equiaxed microstructure, exhibited the least strain rate from 100 to 500 MPa. Despite the similarity in the microstructures of LPBFed-Ti6246, their creep lives varied, in the range of 380 to 440 hours (under the 580 MPa constant stress). Overall, SX2 (SCM)-HT had the longest creep life, while

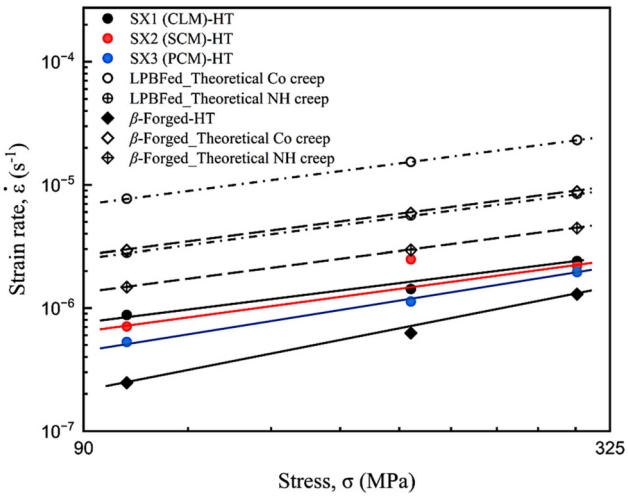

Fig. 8—Comparison of the theoretically predicted Nabarro-Herring (NH) and Coble (Co) creep rates with experimentally observed creep rates at applied low stresses at 500 °C.

SX1 (CLM)-HT exhibited the least creep fracture strain. Therefore, to determine the deformation mechanisms in the respective samples, the step creep tests were further investigated. Figure 6(b) shows the respective creep curves of the step creep tests. The steady-state strain rate ($\dot{\varepsilon}$) usually varies with the applied stress (σ), the absolute temperature (T), and the grain size of the material (d_g) through a relationship that can be expressed in the form of Eq. [2].[28]

$$\dot{\varepsilon} = \dot{\varepsilon}_o \frac{GV_a}{k_o T}\left(\frac{b}{d_g}\right)^p \left(\frac{\sigma}{G}\right)^n \frac{D}{b^2}, \qquad [2]$$

where $\dot{\varepsilon}_o$, G, V_a, k, b, D, p, and n represent the strain rate dependent of temperature and stress, shear modulus, atomic volume, Boltzmann's constant, Burgers vector, diffusion coefficient ($= D_0 \exp(-Q/RT)$, where D_0 is a frequency factor, Q is the activation energy, and R is the gas constant), the inverse grain size exponent, and apparent stress exponent, respectively. In the present study, the grain size (*i.e.,* columnar grain width or hatch distance) and testing temperature do not change; thus, the steady-state strain rate ($\dot{\varepsilon}$) can be considered as a function of the applied stress (σ). Therefore, Eq. 2 can be further expressed as follows:

$$\log \dot{\varepsilon} = \log A + n \log \sigma, \qquad [3]$$

where $A = \dot{\varepsilon}_o \frac{GV_a}{k_o T}\left(\frac{b}{d_g}\right)^p \frac{D}{b^2}$.

In general, the deformation mechanisms in metallic alloys that control high-temperature creep include diffusional creep,[29,30] grain boundary or interface sliding,[31,32] dislocation glide and climb,[33,34] and viscous dislocation glide controlled by dragging of solute atoms or by jogs.[35,36]. One method of knowing which deformation mechanism dominates is by determining the values of the apparent stress exponent (n). The gradient from plotting log $\dot{\varepsilon}$ vs log σ, is used to determine the apparent stress exponent (n) as depicted in Figure 7. For each applied stress, the minimum creep rate value was determined from the steady-state regime where the creep curve exhibited a distinct plateau.

As Figure 7 shows, the values of n fall along two different lines depending on the applied stresses in all the HT LPBFed and the β-forged Ti6246. The apparent stress exponent (n) increased rapidly when the applied stresses exceeded 300 MPa. This breakaway indicates a transition in the occurring deformation mechanisms. It is well established that when $n \cong 1$, the dominant creep process is associated with the Nabarro-Herring-Coble creep (*i.e.,* diffusional creep) or Harper Dorn (H-D) creep mechanisms whereas when $n \cong$ 2-3 the grain boundary sliding mechanism dominates. Above 3, dislocation slip is the dominant deformation mechanism.

For insights on the dominant diffusion mechanism at the applied low stresses (100 − 300 MPa), the theoretical Nabarro-Herring (NH) and Coble (Co) creep rates were calculated using the constitutive equation and available data for β-Ti[37]:

$$\dot{\varepsilon} = A\left(\frac{EbD}{kT}\right)\left(\frac{b}{d}\right)^p \left(\frac{\sigma}{E}\right), \qquad [4]$$

where $A = A_{Co}$or A_{NH} and represent the material constants, calculated Young's modulus, E (at 500 °C) = 4.90×10^4 MPa, $D_L = 1.90 \times 10^{-7} \exp\left(-\frac{153}{RT}\right)$ m^2/s,[37,38] $D_{gb} = 5.40 \times 10^{-17} \exp\left(-\frac{153}{RT}\right)$ m^3/s,[37,38] $b = 2.86 \times 10^{-10}$ m,[37] with $p = 2$ and $D = D_L$ when lattice diffusion dominates the process or $p = 3$ and $D = D_{gb}$ when grain boundary diffusion dominates the process. Figure 8 compares the theoretically predicted NH and Co creep rates to the experimentally observed creep rates in the respective samples. Although the respective NH- and Co-predicted values were all higher than the experimental values, the order of their creep strain rates was almost the same. This observation suggests that NH and Co creep occur concurrently under low applied stress.

To ascertain which mechanism dominates, the creep temperature needs to be considered. Sherby and Wadsworth[39] asserted that Co creep occurs at intermediate temperatures about 0.4 to 0.6 of the melting temperature (T_m), while NH creep is likely to occur at temperatures exceeding $0.7T_m$. Therefore, since the predicted Co creep rate at the test temperature of 500 °C was greater than the NH creep rate, it is reasonable to conclude that Co creep involving grain boundary diffusion dominated at low applied stresses in the present study.

The cross section of each sample was investigated after fracture to understand the effect of the various microstructures on the observed creep behaviors. The microstructures of the cross-sectional samples observed in the build direction (YZ plane) after the creep tests are shown in Figure 9. It was observed that the grains in SX1 (CLM)-HT changed from long pronounced columnar structures to disjointed or fragmented columnar structures (Figure 9(a)). On the other hand, samples SX2 (SCM)-HT and SX3 (PCM)-HT maintained their columnar structures parallel to the build direction as

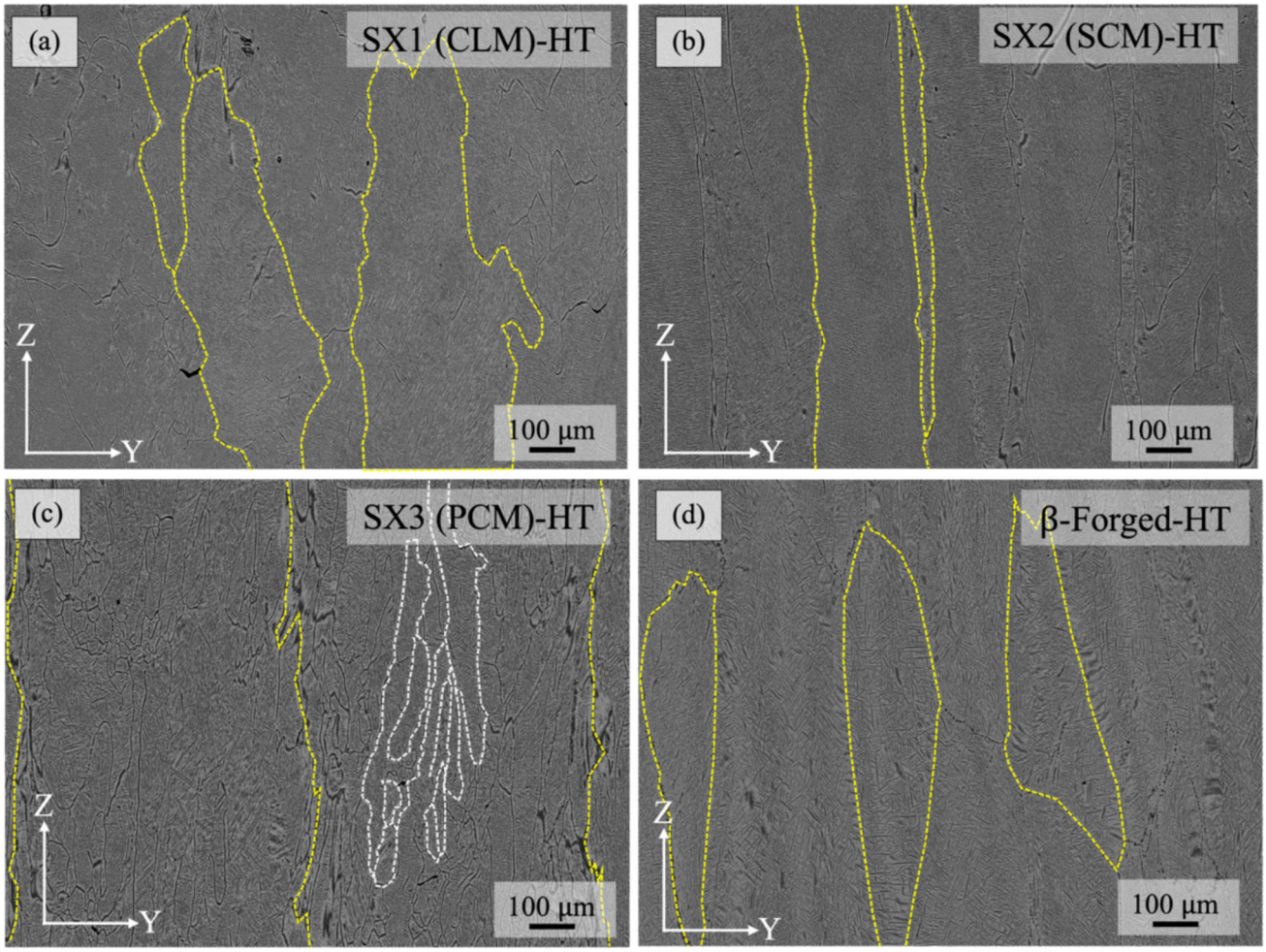

Fig. 9—SEM-BSE images of the cross sections of (*a*) SX1 (CLM)-HT, (*b*) SX2 (SCM)-HT, (*c*) SX3 (PCM)-HT, and (*d*) *β*-Forged-HT samples after fracture observed in the build direction (YZ plane). The yellow-dotted lines indicate the grain boundaries. The elongated substructures were also marked with dotted lines.

depicted in Figures 9(b) and (c), respectively. Interestingly, the width of the columnar structures widened in SX3 (PCM)-HT from 92 μ m to 268 μ m. The threefold increase in the width may suggest grain growth and is corroborated by the formation of elongated substructures (deformed grains) noticed within the thick columnar structures. For the *β*-forged Ti6246, the equiaxed grains were elongated in the direction of the applied stresses as depicted in Figure 9(d).

D. *Fracture Surfaces After Creep Tests*

SEM secondary electron images of the fractured surfaces after the creep tests are shown in Figure 10. The fractured surface of all the LPBFed- and *β*-Forged-HT Ti6246 samples showed numerous ductile dimples and tears. The dimples in SX1 (CLM)-HT, SX2 (SCM)-HT, and SX3 (PCM)-HT were bigger than those in the *β*-Forged-HT. A closer examination of the interior of the dimples in SX1 (CLM)-HT revealed the existence of rings at different depths (inset of Figure 10(a)). These rings are likely melt pool boundaries from different layers of the build.

Furthermore, clear outlines of the laser scan pathways were observed in SX2 (SCM)-HT and SX3 (PCM)-HT as indicated by the dotted lines in Figures 10(b) and (c). This observation suggests delamination, *i.e.,* separation of layers likely from the applied constant pull. In addition, at high magnification, microvoids were observed at the grain boundaries of the *β*-forged-HT Ti6246 as arrowed in the inset of Figure 10(d).

Overall, the creep fracture surface morphologies of the LPBFed and *β*-forged-HT Ti6246 primarily indicate ductile fracture modes.

IV. DISCUSSION

In general, the relatively low mechanical properties of additive manufactured (AM) products are attributed mostly to defects such as pores. These pores are the vulnerable areas where cracks initiate and propagate leading to failure. However, the LPBF AM process boasts of forming fully dense products that help circumvent the effects of pores on mechanical properties, particularly at room temperature. Aside from

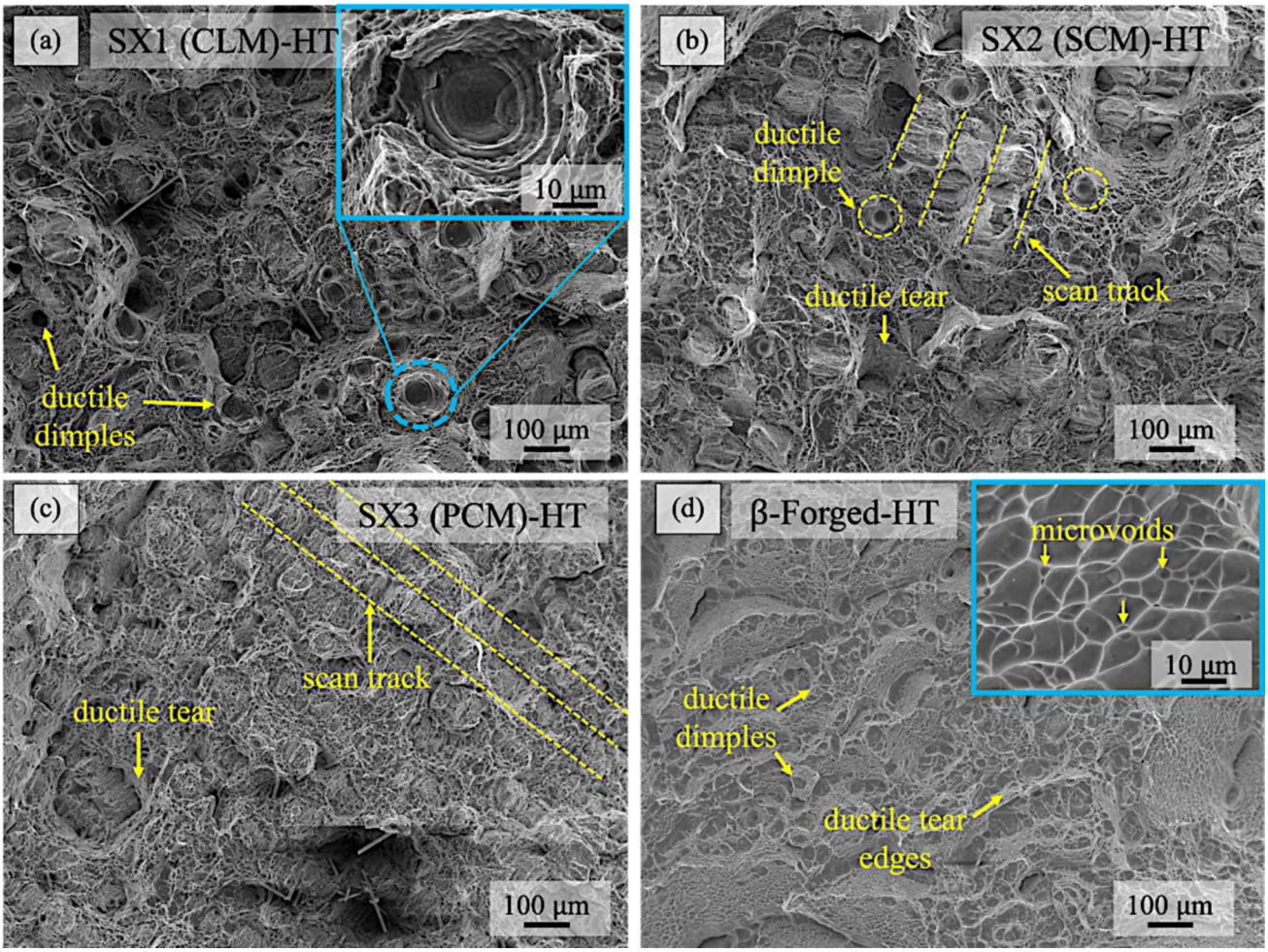

Fig. 10—SEM secondary electron images showing ductile dimples, tears, and microvoids on the fracture surfaces of (*a*) SX1 (CLM)-HT, (*b*) SX2 (SCM)-HT, (*c*) SX3 (PCM)-HT, and (*d*) β-Forged-HT Ti6246.

pores, many factors can influence the mechanical properties of LPBFed products. The present study delved into uncovering and understanding the deformation mechanisms of LPBFed-Ti6246 during creep at 500 °C.

A. *Effect of Microstructural Stability on Creep*

As theoretically predicted, grain boundary diffusion controlled diffusional creep rate at the low applied stresses (100 to 300 MPa) in all the Ti6246 samples. Fundamentally, the contributions of the lattice and grain boundary diffusion creep rates test the stability of microstructures. As such, it is well established that diffusional creep rate hinges on microstructural features, particularly grain size and morphology.[40] As evident in Figure 6, the β-forged-HT Ti6246 with equiaxed grains of average size 138 ± 49 μm exhibited a lower strain rate than the columnar structures of SX1 (CLM)-HT, SX2 (SCM)-HT, and SX3 (PCM)-HT. The observed low strain rate could be attributed to the large equiaxed grain sizes of the β-forged-HT Ti6246 due to the increased distance through which matter had to diffuse for deformation to occur. In addition, the equiaxed

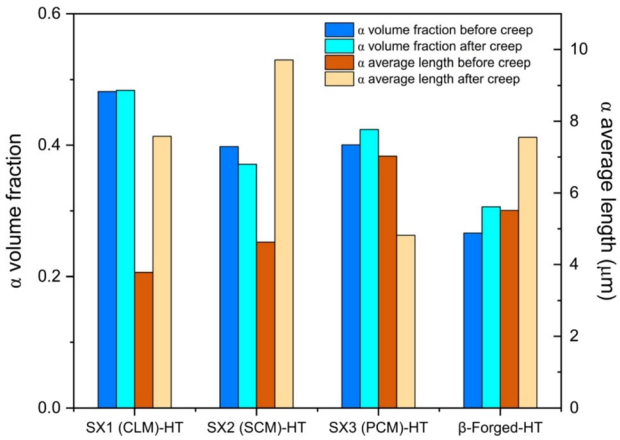

Fig. 11—α phase volume fraction and average length (μm) in the HT LPBFed and the β-forged Ti6246 before and after the creep test at 500 °C.

morphology and large grain sizes in the β-forged-HT Ti6246 presented a more stabilized microstructure because the microstructure homogenously deformed

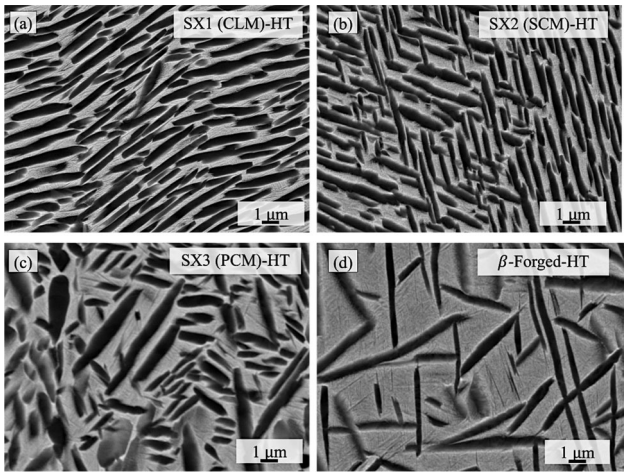

Fig. 12—SEM-BSE images showing the α phase morphologies in (*a*) SX1 (CLM)-HT, (*b*) SX2 (SCM)-HT, (*c*) SX3 (PCM)-HT, and (*d*) the *β*-forged-HT.

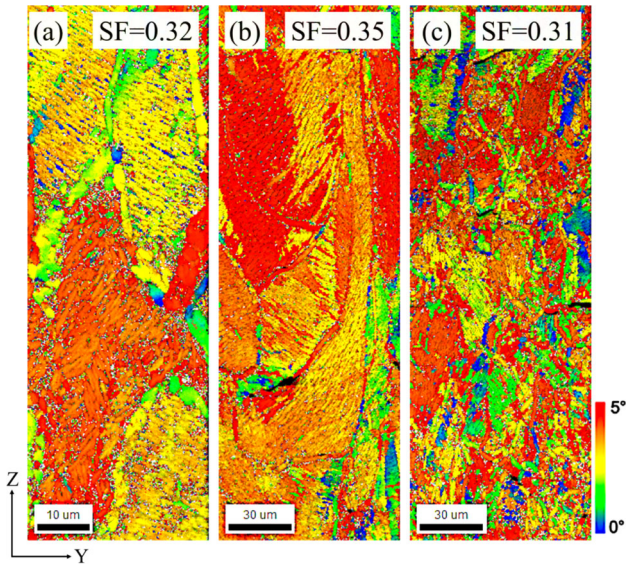

Fig. 13—Schmid factor distribution map of the basal slip system in the α phase of (*a*) SX1 (CLM)-HT, (*b*) SX2 (SCM)-HT, and (*c*) SX3 (PCM)-HT observed from the YZ plane (build direction) parallel to the applied tensile stresses.

under low applied stresses. In other words, diffusion elongated the individual grains in the direction of the applied stresses parallel to the Z-direction (build direction) which was also directly proportional to the macroscopic elongation of the *β*-forged-HT Ti6246 sample (Figure 9(d)).

In the case of the HT LPBFed-Ti6246, the impact of the diffusional creep is quite challenging to explain. However, since grain boundary diffusion, as theoretically determined, controls diffusion rate, the melt pool boundaries can be the most susceptible areas under low applied stresses due to the coarse grain boundary α (or grain boundary-like α), as Figure 4 shows. In Ti alloys, coarser α precipitates decrease local strength mainly because their increased size extends path lengths for dislocation movement. Under creep conditions, these microstructural characteristics could also potentially slide; however, such behavior is generally not observed in additively manufactured Ti alloys characterized by columnar microstructures. This behavior is predominantly noted in equiaxed α microstructures and at temperatures exceeding 700 °C, particularly during superplastic forming operations. Furthermore, although no significant differences were observed in the strain rates of SX1 (CLM)-HT, SX2 (SCM)-HT, and SX3 (PCM)-HT, we surmise that microstructural stability in the HT LPBFed-Ti6246 during diffusional creep depended on the stability of the melt pool boundaries. Evidence suggesting the impact of diffusional creep were seen in SX1 (CLM)-HT (Figure 9(a)), wherein the long pronounced columnar structures changed to disjointed or fragmented columnar structures, and in SX3 (PCM)-HT (Figure 9(c)), characterized by grain growth and grain elongation in the direction of the applied stresses (Z-direction or build direction).

Indeed, the important microstructural feature (average columnar grain width) was about the same for all the LPBFed samples. This is because the hatch distance and powder layer thickness were fixed in all the conditions used. Although we are not able to carry out an appropriate number of scans with different hatch distances to quantitatively justify grain size dependence on the hinted occurrence of diffusional creep controlled by grain boundary diffusion at low applied stresses, the microstructures after creep provided compelling evidence to corroborate our claim. In addition, we justify our assertion by comparing the measured creep rates in the present study to some previous creep studies. Foremost, the observed strain rate and n value in the present study are consistent with studies by Hayes *et al.*[41] on the creep behavior of Ti–6Al–2Sn–4Zr–2Mo (Ti6242) at 565 °C. The authors attributed the rate-controlling mechanism in the Ti6242 at low applied stresses to diffusional creep. Yamane *et al.*[42] inferred a similar rate-controlling mechanism for 25Cr-20Ni stainless steel. According to Ruano *et al.*,[43] one indicator of confirming diffusional creep as the rate-controlling process at low applied stresses is when $n \cong 1$, n tends to increase by a factor of 2 at high applied stresses ($n \cong 3$), in agreement with the present study. Moreover, studies by Kuroda *et al.*[44] and Mitarai *et al.*[31] on the creep performance of LPBFed Ti–6Al–4Nb–4Zr at 600 °C under low applied stress of 137 MPa provide additional support of diffusional creep as the rate-controlling process at low applied stresses when $n \cong 1$. Therefore, it is reasonable to assert that diffusional creep deformation mechanism dominated at low applied stresses in the present study. Section 1.8 on the formation and location of creep voids leading to fracture provides further evidence of the role of diffusional creep at low applied stresses.

B. *Role of the α/β Interface*

It is well documented that precipitates such as the α phase inhibit diffusional creep [45]. However, as the applied stresses increased above 300 MPa, the deformation mechanism in all the HT LPBFed and *β*-forged

Ti6246 deviated from diffusional creep to dislocation slip (with $n \cong 2.3$ (SX1 (CLM)-HT), 3.8 (SX2 (SCM)-HT), 3.1 (SX3 (PCM)-HT), and 3.5 (β-forged-HT)). As elucidated in our previous study,[8] the precipitate sizes in the as-built Ti6246 were quite peculiar. Contrary to several existing studies,[46,47] the low laser power input at fast scan speed combination (fast solidification rate) used in SX3 (PCM) resulted in coarse martensitic precipitates, whereas the high laser power input at slow scan speed (slow solidification rate) in SX1 (CLM) formed refined martensitic precipitates. Figure 11 compares the α-phase volume fraction and average lengths after heat treatment (HT) and creep tests at 500 °C. The volume fraction of the α phase after

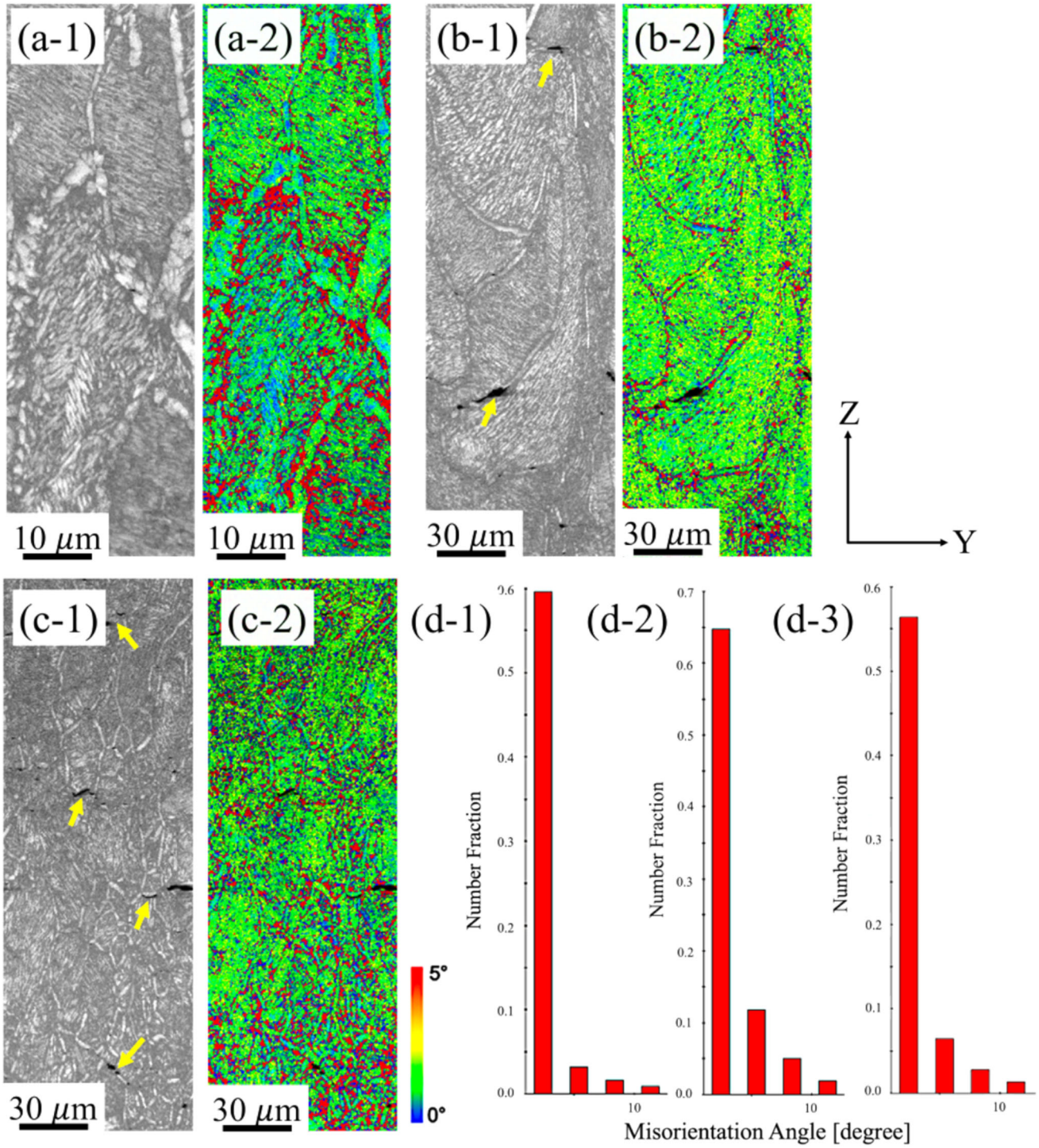

Fig. 14—Image quality and kernel average misorientation (KAM) maps of SX1 (CLM)-HT (*a-1*), (*a-2*), and (*d-1*), SX2 (SCM)-HT (*b-1*), (*b-2*), and (*d-2*), SX3 (PCM)-HT (*c-1*), (*c-2*), and (*d-3*) observed from the YZ plane (build direction) parallel to the applied tensile stresses. Arrows point to cracks in the samples.

HT and creep tests remained nearly the same in SX1 (CLM)-HT, SX2 (SCM)-HT, and SX3 (PCM)-HT as well as the β-forged-HT. Furthermore, the α-phase volume fraction in the respective samples constituted less than 50 pct of the overall microstructure, indicating that the minimum creep rate at stresses greater than 300 MPa depended on the deformation of the α-phase precipitates and the β-phase matrix. Since the α-phase precipitates and the β-phase matrix exhibit different strengths, their interface experiences all the occurring local strains. During deformation, these α/β interfacial regions become barriers to dislocations and as a result, accounting for the deformation resistance under high applied stresses. However, the more dislocations accumulate and interact energy increases, which simultaneously decreases the efficacy of the α/β interfacial regions. The role of the α/β interfacial regions suggest the α-phase volume fraction directly relates to deformation resistance at high applied stresses. This was made evident in the β-forged-HT Ti6246, where the low α-phase volume fraction culminated in a large accelerated deformation at stresses greater than 300 MPa (Figure 6(a)). Along similar lines, Ro *et al.* [48] after investigating several α/β Ti alloys at 500 °C, asserted that the presence of a high α-phase volume fraction tends to decrease the steady-state creep rate in good agreement with the observed deformation behavior in SX1 (CLM)-HT, SX2 (SCM)-HT, and SX3 (PCM)-HT. In all, despite being a classic concept, the notion that the α/β interfacial regions control deformation resistance at high applied stresses remains valid, as shown in this study.

C. *Reasons for the Enhanced Creep Performance in SX2 (SCM)-HT*

Despite the similarities in creep behavior in the HT LPBFed-Ti6246, sample SX2 (SCM)-HT had the longest creep life. A comprehensive understanding of the underlying mechanisms influencing the creep performance of SX2 (SCM)-HT would necessitate additional extensive testing and assessment; nonetheless, we offer some perspectives:

First, the α phase morphology usually serves as the primary predictor of any mechanical property in $\alpha+\beta$ titanium alloys, even when processed through additive manufacturing. Figure 12 presents SEM-BSE high-magnification images of the α precipitates in all the investigated samples.

The morphology of the α precipitates in SX2 (SCM)-HT exhibited no noticeable differences when compared to SX1 (CLM)-HT, SX3 (PCM)-HT, and the β-forged-HT. Similarly, as observed in SX2 (SCM)-HT, both SX1 (CLM)-HT and SX3 (PCM)-HT exhibited continuous and discontinuous grain boundary α, with no distinct differences in their morphologies. The notable distinctions observed in SX2 (SCM)-HT are the highest elongation of the α precipitates and the slight increase of the β phase after creep, as shown in Figure 11. The observed highest elongation of the α precipitates indicates that the sample accommodated the largest amount of dislocation movement and damage accumulation prior to failure. Also, the initial columnar microstructure remained unaltered, with no substructures formed after the creep test. Perhaps this relatively stable microstructure played a crucial role in the observed creep performance of the SX2 (SCM)-HT.

From an alternative viewpoint, it is widely acknowledged that the basal slip system in the α phase is typically regarded as the weak link and is strongly associated with failure mechanisms in Ti alloys. From that perspective, Figure 13 shows the Schmid factor distribution map of the basal slip system in the α phase of the respective LPBFed-Ti6246. The computed Schmid factor of SX2-HT (Figure 13(b)) exhibited a subtle difference from SX1-HT and SX3-HT. Perhaps the difference observed stems from the variant selection in SX2 (SCM)-HT originating from a single grain as

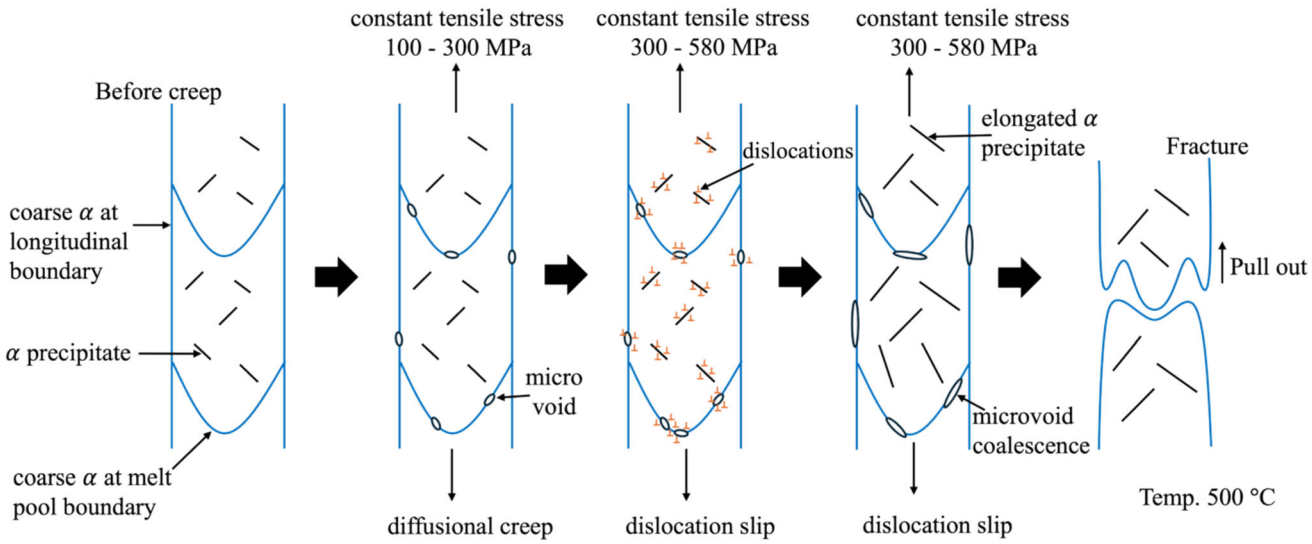

Fig. 15—Schematic of microvoids nucleation, growth, and fracture of the HT LPBFed-Ti6246.

opposed to multiple grains in the other samples. Alternatively, SX2-HT exhibiting a different Schmid factor may also indicate that its creep performance is influenced by factors beyond its microstructure, specifically, the contribution of the SCM texture. Texture is a material property determinant known to influence creep significantly. As previously shown, the as-built texture in SX2 (SCM)-HT suggests that the crystallographic direction of the solidifying β-phase aligned almost in the $< 001 >$ direction, parallel to the build direction (Z-direction) and the applied external tensile stresses as presented in Figure 3(c-1). Therefore, based on the calculated Schmid factors, basal slip is expected to initiate sooner in the SX2-HT, unless perhaps the SCM texture dominated basal slip during the initial stages of plastic deformation leading to the longer creep performance. However, the exact influence of the SCM texture on slip activity and overall creep performance remains unclear. Therefore, further investigation is needed to fully understand the creep performance exhibited by SX2 (SCM)-HT.

D. *Microvoids Nucleation, Growth, and Failure*

To recap, SX1 (CLM)-HT, SX2 (SCM)-HT, and SX3 (PCM)-HT constituted grain boundary α located at the melt pool and longitudinal boundaries. Under creep conditions, these grain boundary α, particularly those that are continuous, undergo the most significant plastic deformation due to dislocation accumulation, resulting in strain localization. This can be easily deduced from the image quality map superimposed with the kernel average misorientation (KAM) map presented in Figure 14, where regions near the grain boundaries (or melt pool boundaries) exhibited increased misorientations after creep. Since the continuous grain boundary α hinders dislocation mobility, the increase in applied stress culminated in increased dislocation pile-ups and stress concentration at these boundaries, ultimately triggering microvoid nucleation. Consequently, all the samples failed due to microvoid nucleation and coalescence forming cracks along the grain boundaries, as arrowed in Figure 14(b-1) and (c-1). Furthermore, the observed variation in ductile dimple sizes can be linked to the plastic zone. As depicted in the insert of Figure 10(d), the microvoids in the β-forged-HT were relatively small, suggesting that the plastic zone was geometrically restricted to the area near the grain boundaries. In the HT LPBFed samples, the formation and growth of the columnar structures involved continuous remelting of layers, which would suggest their plastic zone extended across multiple layers.

In addition, the observed ductile tears in the samples likely occurred at or around α laths. Pilchak *et al.*[49] demonstrated that these ductile tears seen on the fractured surfaces of Ti alloys after creep, as well as the faceted fracture features noted after fatigue tests, are low stress intensity (low ΔK) cracks with sharp tips that propagate along basal planes of the α phase, manifesting as flat, faceted features. Figure 15 presents a schematic illustration of the processes leading to failure in the HT LPBFed-Ti6246.

V. CONCLUSION

In this study, the microstructure, crystallographic texture, and high-temperature creep performance of Ti–6Al–2Sn–4Zr–6Mo wt pct (Ti6246) fabricated using three different LPBF process conditions (SX1—360 W, 800 mm/s; SX2—300 W, 1000 mm/s; SX3—180 W; 1200 mm/s) were investigated. Creep tests on the heat-treated (HT) LPBFed-Ti6246 were carried out at 500 °C. To understand occurring deformation mechanisms, the step creep test was first performed for each sample. The following conclusions were drawn:

- The as-built LPBFed-Ti6246 exhibited columnar microstructures but with three unique crystallographic textures. SX1 formed a crystallographic lamellar-like microstructure (CLM) texture while SX2 and SX3 formed the near $< 001 >$ single crystal-like microstructure (SCM) and polycrystalline microstructure (PCM) texture, respectively.
- Heat treatment (HT) at 885 °C provided sufficient energy and time for the $\alpha\prime$ martensitic phase to decompose to the α phase and grow. The α phases were located within the columnar structures and the melt pool boundaries of SX1 (CLM)-HT, SX2 (SCM)-HT, and SX3 (PCM)-HT.
- At low applied stresses (100–300 MPa), diffusional creep was the dominant deformation mechanism and its resistance depended on the grain size of the tested samples. The β-forged-HT, characterized by large equiaxed grains (138 ± 49 μm), exhibited the lowest strain rate compared to the columnar microstructure of SX1 (CLM)-HT, SX2 (SCM)-HT, and SX3 (PCM)-HT.
- Conversely, dislocation slip governed deformation at high applied stresses (400–580 MPa) and its efficacy depended on the α/β interfaces in the microstructures to impede dislocation mobility.
- The observed disjointed columnar grains in SX1 (CLM)-HT and the deformation of the polycrystalline grains in SX3 (PCM)-HT indicated that the melt pool boundaries were unstable in the LPBFed-Ti6246.
- Nonetheless, SX2 (SCM)-HT exhibited the longest creep life. Compared to SX1 (CLM)-HT and SX3 (PCM)-HT, SX2 (SCM)-HT maintained its continuous columnar structure till fracture. The relatively stable melt pool boundaries coupled with the near $< 001 >$ SCM crystallographic texture of the β matrix in the build direction and parallel to the applied stresses culminated in an improved creep life compared to the reference β-forged-HT Ti6246.
- Ductile dimples and tears and the observation of laser scan tracks characterized the fracture surfaces of the SX1 (CLM)-HT, SX2 (SCM)-HT, and SX3 (PCM)-HT. The failure mode in the SX1 (CLM)-HT, SX2 (SCM)-HT, and SX3 (PCM)-HT was by intergranular ductile fracture from forming creep voids, particularly at melt pool boundaries perpendicular to the applied tensile stresses.

In all, the present study showed that the LPBF process can usefully influence the microstructure and crystallographic texture of the Ti6246 alloy to attain enhanced properties. As evident in SX2 (SCM)-HT, forming a single crystal-like microstructure texture can improve creep performance. In other words, this study reinforces the concept that crystallographic texture could be deliberately controlled using the LPBF process while simultaneously building parts with sophisticated geometries. This serves to benefit the aerospace industry in terms of saving time, energy, and cost in producing needed parts.

ACKNOWLEDGEMENT

Special thanks to Mrs. Nina Kobata of NIMS for all her assistance during the creep tests.

COMPETING INTEREST

On behalf of all authors, the corresponding author states that there is no conflict of interest.

FUNDING

This work was supported by Grants-in-Aid for Transformative Research Area A [grant number JP21H05198] and for Scientific Research [grant number JP23H00235] from the Japan Society for the Promotion of Science (JSPS), and by The Light Metal Educational Foundation (Japan).

DATA AVAILABILITY

Data will be made available on request.

REFERENCES

1. P.V. Cobbinah, R.A. Nzeukou, O.T. Onawale, and W.R. Matizamhuka: *Metals*, 2020, vol. 11, p. 58.
2. T. DebRoy, H.L. Wei, J.S. Zuback, T. Mukherjee, J.W. Elmer, J.O. Milewski, A.M. Beese, A. Wilson-Heid, A. De, and W. Zhang: *Prog. Mater. Sci.*, 2018, vol. 92, pp. 112–224.
3. A. Carrozza, A. Aversa, P. Fino, and M. Lombardi: *J. Alloy. Compd.*, 2021, vol. 870, p. 159329.
4. A. Carrozza, A. Aversa, P. Fino, and M. Lombardi: *Mater. Des.*, 2022, vol. 215, p. 110512.
5. H. Peng, S. Wu, W.H. Kan, S.C.V. Lim, Y. Zhu, and A. Huang: *Scripta Mater.*, 2023, vol. 226, p. 115209.
6. P. Yadav and K.K. Saxena: *Mater. Today: Proc.*, 2020, vol. 26, pp. 2546–57.
7. C. Veiga, J.P. Davim, and A.J.R. Loureiro: *Rev. Adv. Mater. Sci.*, 2012, vol. 32, pp. 133–48.
8. P.V. Cobbinah, S. Matsunaga, Y. Toda, R. Ozasa, M. Okugawa, T. Ishimoto, Y. Liu, Y. Koizumi, P. Wang, T. Nakano, and Y. Yamabe-Mitarai: *Smart Mater. Manuf.*, 2024, vol. 2, p. 100050.
9. TIMET, TIMETAL 6-2-4-6, https://www.timet.com/assets/local/documents/datasheets/aphaandbetaalloys/6246.pdf, Accessed July 4, 2022, 2022.
10. S. Sanchez, P. Smith, Z. Xu, G. Gaspard, C.J. Hyde, W.W. Wits, I.A. Ashcroft, H. Chen, and A.T. Clare: *Int. J. Mach. Tools Manuf*, 2021, vol. 165, p. 103729.
11. K. Hagihara and T. Nakano, JOM, 2021, 1-14.
12. W. Shifeng, L. Shuai, W. Qingsong, C. Yan, Z. Sheng, and S. Yusheng: *J. Mater. Process. Technol.*, 2014, vol. 214, pp. 2660–67.
13. O. Gokcekaya, T. Ishimoto, S. Hibino, J. Yasutomi, T. Narushima, and T. Nakano: *Acta Mater.*, 2021, vol. 212, p. 116876.
14. X. Liu, C. Zhao, X. Zhou, Z. Shen, and W. Liu: *Mater. Des.*, 2019, vol. 168, p. 107677.
15. T. Niendorf, S. Leuders, A. Riemer, H.A. Richard, T. Tröster, and D. Schwarze: *Metall. Mater. Trans. B*, 2013, vol. 44, pp. 794–96.
16. T. Ishimoto, K. Hagihara, K. Hisamoto, S.-H. Sun, and T. Nakano: *Scr. Mater.*, 2017, vol. 132, pp. 34–8.
17. S.H. Lee, M. Todai, M. Tane, K. Hagihara, H. Nakajima, and T. Nakano: *J. Mech. Behav. Biomed. Mater.*, 2012, vol. 14, pp. 48–54.
18. O. Gokcekaya, N. Hayashi, T. Ishimoto, K. Ueda, T. Narushima, and T. Nakano: *Addit. Manuf.*, 2020, vol. 36, p. 101624.
19. T. Ishimoto, S. Wu, Y. Ito, S.-H. Sun, H. Amano, and T. Nakano: *ISIJ Int.*, 2020, vol. 60, pp. 1758–764.
20. M. H. Alluaibi, A. Rusea and V. D. Cojocaru, Romania, 2018, 80.
21. J. Liu, K. Zhang, Y. Yang, H. Wang, Y. Zhu, and A. Huang: *Scr. Mater.*, 2022, vol. 207, p. 114261.
22. J. Liu, K. Zhang, X. Gao, H. Wang, S. Wu, Y. Yang, Y. Zhu, and A. Huang: *Mater. Des.*, 2022, vol. 223, p. 111150.
23. S. L. Corre, R. Forestier, F. Brisset, M. H. Mathon and D. Solas, in Proceedings of the 13th World Conference on Titanium, Wiley Online Library, 2016, pp. 757-764.
24. I. Weiss and S.L. Semiatin: *Mater. Sci. Eng. A, Struct. Mater.: Properties Microstruct. Process.*, 1998, vol. 243, pp. 46–65.
25. Y. Liao, C. Ye, B.-J. Kim, S. Suslov, E. A. Stach and G. J. Cheng, Journal of Applied Physics, 2010, 108.
26. J. Yang, H. Yu, J. Yin, M. Gao, Z. Wang, and X. Zeng: *Mater. Des.*, 2016, vol. 108, pp. 308–18.
27. C. Sauer and G. Luetjering: *J. Mater. Process. Technol.*, 2001, vol. 117, pp. 311–17.
28. T.G. Langdon: *Metall. Mater. Trans. A*, 2002, vol. 33A, pp. 249–59.
29. K. Sotoudeh and P.S. Bate: *Acta Mater.*, 2010, vol. 58, pp. 1909–20.
30. C. Herring: *J. Appl. Phys.*, 1950, vol. 21, pp. 437–45.
31. Y. Yamabe-Mitarai, T. Inoue, T. Kuroda, S. Matsunaga, Y. Toda, T. Matsunaga, T. Ito, R. Ozasa, T. Ishimoto, and T. Nakano: *Mater. Trans.*, 2023, vol. 64, pp. 1175–82.
32. E. Alabort, P. Kontis, D. Barba, K. Dragnevski, and R.C. Reed: *Acta Mater.*, 2016, vol. 105, pp. 449–63.
33. K.R. Athul, U.T.S. Pillai, A. Srinivasan, and B.C. Pai: *Adv. Eng. Mater.*, 2016, vol. 18, pp. 770–94.
34. F. Appel, U. Lorenz, M. Oehring, U. Sparka, and R. Wagner: *Mater. Sci. Eng. A*, 1997, vol. 233, pp. 1–4.
35. T. Suzuki, S. Takeuchi and H. Yoshinaga, Dislocation dynamics and plasticity, Springer Science & Business Media, 2013.
36. F.A. Mohamed and T.G. Langdon: *Acta Metall.*, 1974, vol. 22, pp. 779–88.
37. D.-M. Maps, Pergamon Press, 1982.
38. N. E. W. De Reca and y. C.M. Libanati, Acta Metallurgica, 1968, 16, 1297-1305.
39. O.D. Sherby and J. Wadsworth: *Prog. Mater. Sci.*, 1989, vol. 33, pp. 169–221.
40. G. Malakondaiah and R. Rao: *Def. Sci. J.*, 1985, vol. 35, pp. 201–17.
41. R.W. Hayes, G.B. Viswanathan, and M.J. Mills: *Acta Mater.*, 2002, vol. 50, pp. 4953–63.
42. T. Yamane, N. Genma, and Y. Takahashi: *J. Mater. Sci.*, 1984, vol. 19, pp. 263–69.
43. O.A. Ruano, A.K. Miller, and O.D. Sherby: *Mater. Sci. Eng.*, 1981, vol. 51, pp. 9–16.
44. T. Kuroda, H. Masuyama, Y. Toda, T. Matsunaga, T. Ito, M. Watanabe, R. Ozasa, T. Ishimoto, T. Nakano, and M. Shimojo: *Mater. Trans.*, 2023, vol. 64, pp. 95–103.
45. J.E. Harris: *Met. Sci. J.*, 1973, vol. 7, pp. 1–6.

46. W. Huang and Y. Zhang: *J. Manuf. Process.*, 2019, vol. 42, pp. 139–48.
47. J. Sun, X. Zhu, L. Qiu, F. Wang, Y. Yang, and L. Guo: *Materials Today Communications*, 2019, vol. 19, pp. 277–85.
48. Y. Ro, S. Nakazawa, H. Onodera, K. Ohno, T. Yamagata, I. Tomizuka, and M. Yamazaki: *ISIJ Int.*, 1989, vol. 29, pp. 165–70.
49. A.L. Pilchak, A. Bhattacharjee, A.H. Rosenberger, and J.C. Williams: *Int. J. Fatigue*, 2009, vol. 31, pp. 989–94.